Turk J Elec Engin, VOL.10, NO.2 2002, © TÜBİTAK

Discrete Array Representation of Continuous Space-time Source Distributions

Amir SHLIVINSKI and Ehud HEYMAN
Dept. of Electrical Engineering - Physical Electronics,
Faculty of Engineering, Tel Aviv University-ISRAEL

Abstract

We consider the realization of a continuous space-time source distributions using a sparse non-uniform point-source array. The construction determines the largest possible cells corresponding to the local source parameters in order to obtain a sparse array, while meeting an error criterion on the pulsed radiation pattern. The scheme is applied for the realization of collimated short-pulse beam fields. The error criterion is imposed within the main beam direction, while outside this region the relative realization error can be large but it is negligible since the field there is small compared to the main beam field.

Key Words: *slant stack transform, ultra-wide band short-pulse signals, continuous space-time source distribution, sparse non-uniform point source array*

1. Introduction

The increased interest in the radiation and reception of ultra-wideband short-pulse (UWB-SP) signals has made an impact on the design of UWB antennas and in particular on UWB-SP array antennas that are capable of radiating and steering collimated short pulsed fields (pulsed beams). Such arrays are referred to as "pulsed-antenna arrays," "transient arrays" or "delay arrays" [1-7]. Most applications, for example those involving high resolution two- and three-dimensional imaging, require very large arrays that must be properly thinned to avoid an unrealistic cost, complicated electronics, and managing of huge data-flow for real-time processing. However, array thinning based on conventional narrowband (frequency domain) considerations applied at the highest frequency in the signal spectrum leads to unnecessarily ultra-dense arrays since it does not utilize the fact that the resulting wave-fields are localized in space *and* in time. The limitations on the array geometry in this frequency domain approach are due to phase-interference (kinematic) phenomena and are therefore irrelevant in the SP field regime. The kinematic properties of SP arrays have been studied recently in [4, 7]. Reference [7] dwells on the transition of the kinematic phenomena from the narrowband regime to the UWB-SP regime and demonstrates in particular how the grating lobes that characterize narrowband arrays are replaced by "cross-pulse lobes" that depend on the pulse repetition rate. This gives rise to possible sparse arrays whose inter-element spacing is *much larger* than the wavelengths in the frequency band and basically does not suffer from severe side lobe problems.

A different approach is considered in the present paper which is concerned with an array realization of continuous source distributions for collimated short-pulse beam fields. Several classes of such wave-fields have been introduced in the last two decades (for a review, see the Introduction in [8]). Our goal is to synthesize such fields using an array of pulsed point sources that will reconstruct the time-dependent far

field pattern within a certain cone around the "main beam" direction and within a specified error. It is required that the array will have the smallest number of elements possible.

The analytically specified continuous sources are typically characterized by non-uniform space-time distributions, hence each array-element in the discretized formulation must compensate for both the amplitude and the waveform variations of the idealized (i.e., continuous) distribution within the local cell. This sets a limit on the dimensions of each one of the cells in the array as a function of the local pulse-length and of the transverse variation of the source-waveform. The final non-uniform array geometry (and thus the number of its elements) is then determined by weighting the errors from the individual cells in order to meet the total error criterion within a given space-time window; the cell dimensions (and thereby the array sparsity) are proportional to the error level allowed.

The general conditions derived in this approach are applied for the array-realization of the so called complex source pulse beam (CSPB also termed iso-diffracting pulsed beam) [8]. Compared with a conventional monochromatic array design, the resulting non-uniform array is shown to be ultra-sparse with inter-element spacing much larger than the wavelength of the frequencies in the band.

The paper is organized as follows. The problem is formulated in Section 2 in term of the slant stack transform (SST) of the continuous space-time source distribution [9-12]. In Section 3, the continuous distribution is divided into cells and the contribution of each cell to the time-dependent radiation pattern is analyzed locally. These results are compared in Section 4 with the radiation pattern of an array of pulsed point-sources where it is required to use the smallest number of array elements while reconstructing the radiation patterns within a certain cone around the "main beam" direction. Imposing this error constraint and maximizing the cell's size yields expressions for the local cell's dimensions and to the design algorithm (Section 4.3). An example of a PB array realization is presented in Section 5 followed by concluding remarks in Section 6.

2. Problem Formulation: Array Realization of Continuous Source Distribution

We are interested in the far field $u(\boldsymbol{r},t)$ radiated by a pulsed source distribution $Q(\boldsymbol{r},t)$ in a uniform three-dimensional space with wavespeed c. The field satisfies the time-dependent wave equation

$$\left(\nabla^2 - \frac{1}{c^2}\frac{\partial^2}{\partial t^2}\right) u(\boldsymbol{r},t) = -Q(\boldsymbol{r},t), \quad Q(\boldsymbol{r},t) = q(\boldsymbol{x},t)\delta(z), \tag{1}$$

where $\boldsymbol{r} = (\boldsymbol{x}, z)$ with $\boldsymbol{x} = (x_1, x_2)$ being the coordinates transverse to z. It is assumed that $Q(\boldsymbol{r},t)$ is a surface source distribution confined in the $z = 0$ plane within a disk of radius R_0 centered at the origins such that

$$q = 0 \quad \text{for} \begin{cases} |\boldsymbol{x}| > R_0 \\ t \notin (0,T). \end{cases} \tag{2}$$

It is also assumed that the source generates a collimated pulsed beam field that propagates essentially along the z axis.

Our goal is to synthesize the field using an array of point sources that will reconstruct the far field pattern within a certain cone around the "main beam" direction z and up to a specified error. It is required that the array will have the smallest number of elements possible.

The time-dependent radiation pattern of the continuous source distribution is described by the time derivative of the slant stack transform (SST) of q, defined by

$$\widetilde{q}(\boldsymbol{\xi},t)=\int d^2x\, q(\boldsymbol{x},t+\boldsymbol{\xi}\cdot\boldsymbol{x}/c), \tag{3}$$

with $\boldsymbol{\xi}=(\xi_1,\xi_2)$. This standard operation has been introduced in [9, 10, 11, 12] in connection with the time dependent plane wave spectrum and radiation pattern, and has also been studied extensively in [12]. Having calculated $\widetilde{q}(\boldsymbol{\xi},t)$, the field in the far radiation zone is given by

$$u(\boldsymbol{r},t)\Big|_{r\to\infty}=\frac{\partial_t\widetilde{q}(\boldsymbol{\xi},t-r/c)}{4\pi r}\Big|_{\boldsymbol{\xi}=\widehat{\boldsymbol{r}}_\perp} \tag{4}$$

where $\widehat{\boldsymbol{r}}_\perp=\widehat{\boldsymbol{r}}-\widehat{\boldsymbol{z}}(\widehat{\boldsymbol{r}}\cdot\widehat{\boldsymbol{z}})=\sin\theta(\cos\phi,\sin\phi)$ is the projection of the observation direction $\widehat{\boldsymbol{r}}$ onto the $z=0$ plane. We may therefore refer to $\partial_t\widetilde{q}(\boldsymbol{\xi},t)$ as the time domain radiation pattern.

In the array realization, the source distribution is described by a non uniform array of point sources $Q_n(t)$ located at points $\boldsymbol{x}_n$ in the $z=0$ plane where n is an index. The radiation pattern produces by this array is given by (4) with

$$\widetilde{q}^{\,\text{array}}(\boldsymbol{\xi},t)=\sum_n Q_n(t+\boldsymbol{\xi}\cdot\boldsymbol{x}_n/c). \tag{5}$$

Our goal is to determine the sparsest array such that (5) will provide a valid representation for (3) within a given cone $\theta<\Theta$ about the z-axis (see (20) and (22)), where Θ typically depends on the application. In (18a) it will be shown to first order that Q_n are given by

$$Q_n(t)=S_n q(\boldsymbol{x}_n,t) \tag{6}$$

where S_n is the area on the cell adjacent to $\boldsymbol{x}_n$.

3. Local Evaluation of the SST

Following the discussion above, we shall quantify in this section the radiation-pattern error introduced by the array-realization of the continuous distribution, and thus to establish criteria for the array design. We therefore divide the continuous distribution into a non-uniform array of cells that are centered at $\boldsymbol{x}_n$, and then calculate $\widetilde{q}$ of (3) as a sum of the cell contributions. The resulting pattern will then be compared to that of the point source array in (5) and the error criteria will be imposed in Section 4.

The SST $\widetilde{q}$ in (3) is given now by

$$\widetilde{q}(\boldsymbol{\xi},t)=\sum_n \widetilde{q}_n(\boldsymbol{\xi},t) \tag{7}$$

where the SST contribution of an individual cell is

$$\widetilde{q}_n(\boldsymbol{\xi},t)=\int_{\boldsymbol{x}\in\, n\text{th cell}} d^2x\; q(\boldsymbol{x},t+\boldsymbol{\xi}\cdot\boldsymbol{x}/c) \tag{8a}$$

$$=\int_{|\eta_i|<d_{n_i}} d^2\eta\; q(\boldsymbol{x}_n+\mathbf{O}_n^T\boldsymbol{\eta},t_n+\boldsymbol{\xi}_n\cdot\boldsymbol{\eta}/c). \tag{8b}$$

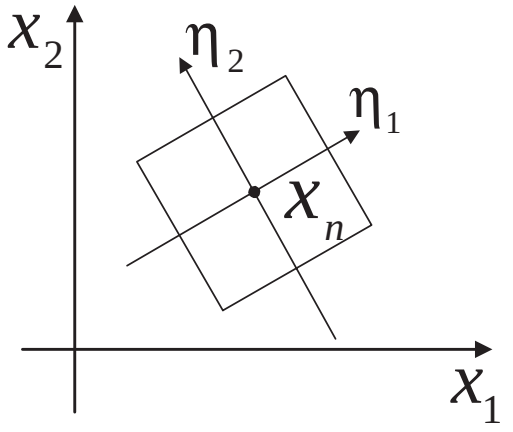

Figure 1. Single cell coordinate system

In (8b) we introduced conveniently the local coordinates $\boldsymbol{\eta} = (\eta_1, \eta_2)$ around $\boldsymbol{x}_n$

$$\boldsymbol{x} = \boldsymbol{x}_n + \boldsymbol{\eta}\mathbf{O}_n, \qquad \mathbf{O}_n = \begin{bmatrix} \cos\psi_n & \sin\psi_n \\ -\sin\psi_n & \cos\psi_n \end{bmatrix}, \tag{9}$$

where $\mathbf{O}_n$ is a rotation matrix at an angle ψ_n such that the local coordinates $\boldsymbol{\eta}$ coincide with the cell orientation (see Figure 1), and $d_{n_1} \times d_{n_2}$ are cell's dimensions. In this system $t_n = t + \boldsymbol{\xi} \cdot \boldsymbol{x}_n/c$ is the reference time at the cell center and $\boldsymbol{\xi}_n = \boldsymbol{\xi}\mathbf{O}_n^T$ denotes the rotated spectral coordinates, with T denoting the transpose.

Next we derive an approximate expression for the SST contribution (8) of each cell. We first express the space-time source distribution in the cell in a format that is amenable for the SST calculations (Section 3.1), and then evaluate the local SST (Section 3.2).

3.1. Local model for the field in a cell

Our first step is to obtain a simplified expression for the time-dependent field in the vicinity of $\boldsymbol{x}_n$ that is amenable for a closed form calculation of $\widetilde{q}_n$. It is convenient to start in the frequency domain where field constituents are denoted by the caret and are related to the time domain constituents via

$$u(t) = \frac{1}{2\pi}\int_{-\infty}^{\infty} d\omega\, e^{-i\omega t}\widehat{u}(\omega). \tag{10}$$

We express the initial frequency domain field in the vicinity of $\boldsymbol{x}_n$ as

$$\widehat{q}(\boldsymbol{x},\omega) = \widehat{q}(\boldsymbol{x}_n,\omega)e^{i\Phi_n(\boldsymbol{\eta},\omega)}, \quad \text{i.e. } \Phi_n(\boldsymbol{\eta},\omega)|_{\boldsymbol{\eta}=\mathbf{0}} = 0. \tag{11}$$

Next we expand Φ_n in a Taylor series in ω and η near $\boldsymbol{x_n}$. We also assume that Φ_n is predominantly linear in ω, i.e. it mainly describes a distributed delay. Thus, for small η

$$\Phi_n(\boldsymbol{\eta},\omega) = \omega T_n(\boldsymbol{\eta}) + \ldots \tag{12a}$$

$$T_n(\boldsymbol{\eta}) = \sum_i T_{n_i}\eta_i + \tfrac{1}{2}\sum_{i,j} T_{n_{ij}}\eta_i\eta_j + \ldots \tag{12b}$$

with $T_{n_i} = \partial_\omega \partial_{\eta_i} \Phi_n$, $T_{n_{ij}} = \partial_\omega \partial^2_{\eta_i \eta_j} \Phi_n$, and $i = 1, 2$. In (12a) we neglected terms of order $\eta, \eta^2, \ldots$ that describe a frequency-independent spatial envelope, and terms of order $\omega^2 \eta \ldots, \omega^3 \eta, \ldots$ that introduce dispersive components into Φ_n. Thus $T_n(\boldsymbol{\eta})$ represents a non-dispersive "delay" but it may be complex so that it describes the amplitude variation near $\boldsymbol{x}_n$ as will be explained next.

In order to accommodate the complex "delay" $T_n(\boldsymbol{\eta})$ we utilize the analytic signal formulation. Referring to (10), the analytic signal $\overset{+}{u}$ corresponding to a given real signal $u(t)$ for $t \in \mathbb{R}$, and with frequency spectrum $\widehat{u}(\omega)$, is defined via the one-sided inverse Fourier transform

$$\overset{+}{u}(\tau) = \frac{1}{\pi} \int_0^\infty d\omega \, e^{-i\omega\tau} \widehat{u}(\omega) \, . \tag{13}$$

This integral defines an analytic function in the complex τ plane whose region of analyticity depends on the asymptotic behavior of $\widehat{u}$: if $\widehat{u}(\omega) \sim \mathcal{O}(e^{-\alpha\omega})$ for $\omega \to \infty$ where $\alpha > 0$ is a constant then $\overset{+}{u}(\tau)$ is analytic for $\operatorname{Im}\tau < \alpha$.

Applying (13) to (11) with (12a) yields for $\boldsymbol{x} \approx \boldsymbol{x}_n$ (i.e., for small $\boldsymbol{\eta}$)

$$q(\boldsymbol{x}, t) \approx \operatorname{Re} \overset{+}{q}(\boldsymbol{x}_n, t - T_n(\boldsymbol{\eta})). \tag{14}$$

The real part of $T_n(\boldsymbol{\eta})$ represents a pure delay (positive or negative) relative to the signal at $\boldsymbol{x}_n$, but the imaginary part causes a change of the signal and of its magnitude. For $\boldsymbol{\eta}$ such that $\operatorname{Im} T_n(\boldsymbol{\eta}) \gtrless 0$ the signal decays or grows relative to its value at $\boldsymbol{x}_n$, respectively. As follows from the discussion in (13), $\operatorname{Im} T_n(\boldsymbol{\eta})$ should be smaller than some positive constant (say $\alpha > 0$) that is typical large for smooth $q(x, t)$. Thus the smoothness of q determines the range of validity of (14) about $\boldsymbol{x}_n$.

3.2. Local evaluation of the SST

Next, we insert (14) with (12b) to the SST integral (8) and expand the integrand into a Taylor series around $t_n = t + \boldsymbol{\xi} \cdot \boldsymbol{x}_n / c$. Collecting terms of equal order in η yields

$$q(\boldsymbol{x}_n + \mathbf{O}_n^T \boldsymbol{\eta}, t_n + \boldsymbol{\xi}_n \cdot \boldsymbol{\eta}/c) = \sum_j {}_j q_n(\boldsymbol{\eta}, t) \tag{15}$$

where the left-hand subscripts denotes the index of the series in (15) with ${}_j q_n \sim \mathcal{O}(\eta^j)$, and

$${}_0 q_n(\boldsymbol{\eta}, t) = \operatorname{Re}\big\{ \overset{+}{q}(\boldsymbol{x}_n, t_n) \big\}, \tag{16a}$$

$${}_1 q_n(\boldsymbol{\eta}, t) = \operatorname{Re}\big\{ \overset{+}{q}{}^{(1)}(\boldsymbol{x}_n, t_n) \sum_i (\xi_{n_i}/c - T_{n_i}) \eta_i \big\} \tag{16b}$$

$${}_2 q_n(\boldsymbol{\eta}, t) = \tfrac{1}{2} \operatorname{Re}\big\{ - \overset{+}{q}{}^{(1)}(\boldsymbol{x}_n, t_n) \sum_{i,j} T_{n_{ij}} \eta_i \eta_j + \overset{+}{q}{}^{(2)}(\boldsymbol{x}_n, t_n) \big[\sum_i (\xi_{n_i}/c - T_{n_i}) \eta_i \big]^2 \big\} \tag{16c}$$

with $t_n = t + \boldsymbol{\xi} \cdot \boldsymbol{x}_n / c$ (see (8)). Here ξ_{n_i} with $i = 1, 2$ denotes the ith coordinate of $\boldsymbol{\xi}_n$ as defined after (9) and $\overset{+}{q}{}^{(k)} \equiv \partial_t^k \overset{+}{q}$. Performing the integration in (8b) within the cell, using (15) and (16), yields a series approximation for $\widetilde{q}_n$

$$\widetilde{q}_n(\boldsymbol{\xi}, t) = {}_0\widetilde{q}_n(\boldsymbol{\xi}, t) + {}_2\widetilde{q}_n(\boldsymbol{\xi}, t) + \mathcal{O}(d^6) \ , \tag{17}$$

where $\widetilde{{}_{j}q}_n \sim \mathcal{O}(d^{j+2})$

$$\widetilde{{}_{0}q}_n(\boldsymbol{\xi},t) = S_n \mathrm{Re}\left\{\overset{+}{q}(\boldsymbol{x}_n,t_n)\right\} \tag{18a}$$

$$\widetilde{{}_{2}q}_n(\boldsymbol{\xi},t) = \frac{S_n}{24}\sum_i d_{n_i}^2 \,\mathrm{Re}\left\{(\xi_{n_i}/c - T_{n_i})^2 \overset{+}{q}{}^{(2)}(\boldsymbol{x}_n,t_n) - T_{n_{ii}} \overset{+}{q}{}^{(1)}(\boldsymbol{x}_n,t_n)\right\} \tag{18b}$$

with $S_n = d_{n_1} d_{n_2}$ is the area of the nth cell.

4. Error Analysis of the Point-Sources-Array Realization

4.1. Error criteria

From (18a), the first term in (17) represents an isotropic point source contribution, thus justifying the point source array realization in (5)–(6). The second term represents the effects of the finite cell size and of the linear and quadratic variations of T_n over the cell (recall that in general T_{n_i} and $T_{n_{ii}}$ are complex as discussed in connection with (14)). This second term will therefore be used to quantify the radiation-pattern error introduced by the realization of the continuous source distribution using the sparse point sources array. The array geometry will then be determined by setting a given bound on the error for all observation directions within a specific cone $\theta \le \Theta$ about the z-axis (see discussion after (5)).

Below we shall consider separately the error $\bar{e}_n(\boldsymbol{\xi})$ introduced by neglecting the second term in (17) in the individual cell contribution and then the total error of the array realization $e(\boldsymbol{\xi})$.

The relative error introduce by describing a single cell contribution using a point source as in the first term in (17) (see also (6)) is given by

$$\bar{e}_n(\boldsymbol{\xi}) \equiv \frac{\|\widetilde{q}_n(\boldsymbol{\xi},t) - \widetilde{{}_{0}q}_n(\boldsymbol{\xi},t)\|}{\|\widetilde{q}_n\|} \simeq \frac{\|\widetilde{{}_{2}q}_n(\boldsymbol{\xi},t)\|}{\|\widetilde{{}_{0}q}_n\|} \tag{19}$$

where in the second equality we used (17). It is required that

$$\bar{e}_n(\boldsymbol{\xi}) \le \bar{\epsilon} \qquad \forall\ |\boldsymbol{\xi}| < \sin\Theta \tag{20}$$

where $\bar{\epsilon}$ is a prescribed bound.

Similarly, the total error introduced by the point source realization, normalize relative to the radiation pattern along the main beam axis is given by

$$e(\boldsymbol{\xi}) \equiv \frac{\|\widetilde{q}(\boldsymbol{\xi},t) - \widetilde{q}^{\,\mathrm{array}}(\boldsymbol{\xi},t)\|}{\|\widetilde{q}(\mathbf{0},t)\|} \simeq \frac{\|\sum_n \widetilde{{}_{2}q}_n(\boldsymbol{\xi},t)\|}{\|\widetilde{q}(\mathbf{0},t)\|} \tag{21}$$

where $\widetilde{q}^{\,\mathrm{array}}$ is defined in (5). It is required that

$$e_n(\boldsymbol{\xi}) \le \epsilon \qquad \forall\ |\boldsymbol{\xi}| < \sin\Theta \tag{22}$$

where ϵ is another prescribed bound. Clearly one should choose $\epsilon \ll \bar{\epsilon}$.

4.2. Error analysis

The norm in the definitions above can be of any type: It should be chosen according to the observables (i.e., field-detectors) that are used to quantify the radiation pattern (e.g. $\mathbb{L}_1$, $\mathbb{L}_2$, or $\mathbb{L}_\infty$ norms). In the example of Section 5 we use the $\mathbb{L}_2$ (energy) norm.

Using (18b) and the triangle inequality for the norm in the numerator of (19) and noting also from (18a) that $\|\widetilde{\mathcal{q}}_n\| = S_n\|q(\boldsymbol{x}_n,t)\|$ we obtain

$$\bar{e}_n \le \sum_i d_{n_i}^2 \frac{E_{n_i}(\xi_{n_i})}{\|q_n\|} \tag{23}$$

with

$$E_{n_i}(\xi_{n_i}) \le \frac{1}{24}\big\{|\xi_{n_i}/c - T_{n_i}|^2\|q_n^{(2)}\| + |T_{n_{ii}}|\|q_n^{(1)}\|\big\} \tag{24}$$

where $\|q_n\| \equiv \|q(\boldsymbol{x}_n,t)\|$, $\|q_n^{(1)}\| = \|\partial_t q(\boldsymbol{x}_n,t)\|$, etc. In the derivation, the norms of the analytic signals in (18) were evaluated on the real argument axis where for the $\mathbb{L}_2$ norm we have $\|\overset{+}{q}\| = \sqrt{2}\|q\|$.

Maximizing the cell size $S_n = d_{n_1}d_{n_2}$ subject to the error constraint in (20) yields the cell dimensions

$$d_{n_i}(\boldsymbol{x}_n) = \min_{|\boldsymbol{\xi}|<\sin\Theta}\left[\frac{\bar{\epsilon}}{2}\frac{\|q_n\|}{E_{n_i}(\xi_{n_i})}\right]^{\frac{1}{2}},\ i=1,2 \tag{25}$$

From (24), the largest E_{n_i} in the range $|\boldsymbol{\xi}| < \sin\Theta$ is obtained for $|\boldsymbol{\xi}| = \sin\Theta$. Maximization on the azimuthal spectral angle ψ_n is problem dependent, hence we shall use a typical value: $\boldsymbol{\xi}_n = (\xi_{n_1},\xi_{n_2}) \simeq (\frac{1}{\sqrt{2}},\frac{1}{\sqrt{2}})\sin\Theta$. The result in (25) yield the largest cell that can be described by a point source, as a function of the local source properties.

Next we shall consider the constraint (22) on the total radiation pattern error. Eq. (21) defines the total error as a sum of the single cell errors and hence it does not relate directly to the single cell dimensions. We therefore rearranging (21) as

$$e(\boldsymbol{\xi}) \simeq \Big\|\frac{\sum_n e_n(\boldsymbol{\xi})\widetilde{\mathcal{q}}_n}{\|\widetilde{\mathcal{q}}_n\|}\Big\| \le \epsilon \tag{26a}$$

where

$$e_n(\boldsymbol{\xi}) \equiv \frac{\|\widetilde{\mathcal{q}}_n(\boldsymbol{\xi},t)\|}{\|\widetilde{q}(\mathbf{0},t)\|} \le S_n\sum_i d_{n_i}^2\frac{E_{n_i}(\xi_{n_i})}{\|\widetilde{q}(\mathbf{0},t)\|} \tag{26b}$$

is the single element error normalized to $\widetilde{q}(\mathbf{0},t)$, and the last inequality follows from (18b) with (24). It will be required that

$$e_n(\boldsymbol{\xi}) \le \widetilde{\epsilon} \qquad \forall\ |\boldsymbol{\xi}| < \sin\Theta \qquad \text{and } \forall\, n \tag{27}$$

where $\widetilde{\epsilon}$ is a parameter to be determined. To find a bound on $\widetilde{\epsilon}$ we use norm inequality to $e(\boldsymbol{\xi})$ obtaining $e(\boldsymbol{\xi}) \le \widetilde{\epsilon}\Big\|\sum_n \widetilde{\mathcal{q}}_n/\|\widetilde{\mathcal{q}}_n\|\Big\|$. Next we recall that the error criterion should be imposed outside the main beam direction (for $\boldsymbol{\xi} \not\approx 0$). Noting that in this region the delayed-error terms $\widetilde{\mathcal{q}}_n$ are not coherent it follows that $\Big\|\sum_n \widetilde{\mathcal{q}}_n/\|\widetilde{\mathcal{q}}_n\|\Big\| \sim \mathcal{O}(1)$, suggesting that in this range $\widetilde{\epsilon} \sim \epsilon$. Using this value of $\widetilde{\epsilon}$ in (27) together with the last term on the right hand side of (26b) and maximizing the cell area as in (25) yields

$$d_{n_i}(\boldsymbol{x}_n) = \min_{|\boldsymbol{\xi}|<\sin\Theta}\left[\Big(\frac{\epsilon}{2}\|\widetilde{q}(\mathbf{0},t)\|\Big)^{1/4}\frac{\big[E_{n_1}(\xi_{n_1})E_{n_2}(\xi_{n_2})\big]^{1/8}}{\big[E_{n_i}(\xi_{n_i})\big]^{1/2}}\right] \tag{28}$$

where as noted after (25) may shall use a typical value $\boldsymbol{\xi}_n \simeq (\frac{1}{\sqrt{2}},\frac{1}{\sqrt{2}})\sin\Theta$.

4.3. Array design considerations

Equation (25) and (28) provides two constraints on the cell size d_{n_i}, $i = 1, 2$ and for all n. The values of d_{n_i} obtained from (25) sets an upper limit on the cell size for which the second order analysis is valid, whereas those obtained via (28) are concerned only with meeting the constraint on the total radiation pattern. For focusing apertures, $q(\boldsymbol{x}, t)$ is typically large near the center hence the condition (28) dominates for this elements. Consequently, the dimensions of the central cells are found from (28) yielding a rather dense array. Far from the center q weakens and the cell dimensions implied by (28) grow until they disagree with the condition in (25) which then becomes operative. The array construction starts therefore from the center and proceeds outward where at each step one calculates $d_{n_{1,2}}(\boldsymbol{x}_n)$ via the condition in (25) or (28).

When the procedure above is applied to scanning arrays, the array sparsity is determined by the most restrictive constraints corresponding to all the possible scan directions within a given range. Consider the case where the array should stir a given collimated pulsed beam (PB) for all directions within a cone of angle $\theta_{\max}$ about the z axis. The analysis for each direction proceeds essentially as discussed above, but by considering all possible scan directions one finds that the resulting array geometry is almost the same as obtained for a fixed broadside array that radiates a PB along the z-axis. In fact, the size of the array should be increased by a factor $1/\cos\theta_{\max}$, so as to obtain the same effective aperture at the largest scan angle, but the interelement spacing should remain essentially the same so as to accommodate all the scan directions within the cone.

To be more specific, for a scan in the direction (θ_0, ϕ_0), the complex delay $T(\boldsymbol{\eta})$ (see Section 3.1) is augmented by a linear delay $T(\boldsymbol{x}) = c^{-1}[x_1 \sin\theta_0 \cos\phi_0 + x_2 \sin\theta_0 \sin\phi_0]$. For simplicity let the local cell geometry be oriented such that η_1 coincides with the scan direction. Consequently, each one of the the parameters T_{n_1} of (12b) is augmented by $c^{-1}\sin\theta_0$. It then follows from (24) that E_{n_1} is minimized for observations along the beam axis where $\xi_{n_1} = \sin\theta_0$. Substituting E_{n_1} in Eqs. (25) and (28) and considering observation directions within a cone Θ about the PB direction $(\theta_0, \phi_0 = 0)$, one obtains essentially the same realization constraints as obtained for radiation along the z-axis. Finally, these considerations should be repeated for all scanning directions within the $\theta_{\max}$ cone. For this reasons the example of Section 5 below considers only the realization for a broadside radiating array.

5. Example: Iso-Diffracting Source Distribution

We consider a circular symmetry pulsed aperture distribution of the form

$$q(\boldsymbol{x}, t) = \mathrm{Re}\overset{+}{f}[t - i|\boldsymbol{x}|^2/2bc], \tag{29}$$

where $\overset{+}{f}(t)$ can be any analytic signal and b is a positive parameter. In [10] this distribution has been termed "iso-diffracting" since all its frequency components have the same collimation distance b. Indeed, looking at its frequency spectrum for $\omega > 0$,

$$\widehat{q}(\boldsymbol{x}, \omega) = \widehat{f}(\omega) \exp\{-\omega|\boldsymbol{x}|^2/2bc\} \tag{30}$$

where $\widehat{f}(\omega)$ is the spectrum of $\overset{+}{f}(t)$, one finds that the width of the Gaussian $\boldsymbol{x}$-distribution varies with ω like $\sqrt{bc/\omega}$, hence its Rayleigh (collimation) distance is given by b for all ω.

In the examples below we choose $\overset{+}{f}$ to be the n-times differentiated analytic-δ signal

$$\overset{+}{f}(t) = \overset{+}{\delta}{}^{(n)}(t - i\bar{T}_0/2) = \mathrm{Re}\left\{\frac{(-)^n n!}{\pi i(t - i\bar{T}_0/2)^{n+1}}\right\} \tag{31}$$

where $\bar{T}_0 > 0$ is a parameter that defines the pulse length. To understand the properties of (29) we use $n = 2$ in (31) and write (29) explicitly for this case, obtaining

$$q(\boldsymbol{x}, t) = \mathrm{Re}\,\overset{+}{\delta}{}^{(2)}(t - i\gamma/2) = \frac{\gamma}{\pi}\frac{\left[3t^2 - (\gamma/2)^2\right]}{\left[t^2 + (\gamma/2)^2\right]^3} \tag{32}$$

where $\gamma = \bar{T}_0 + |\boldsymbol{x}|^2/bc$. Analyzing the waveform in (32) one observes that the pulse length is given by γ and hence it grows with $|\boldsymbol{x}|$. In addition, the waveform decays as γ grows, hence the half-amplitude diameter that describes the decay in $|\boldsymbol{x}|$ is found to be $W_0 = 1.02\sqrt{c\bar{T}_0 b}$. Plots of $q(\boldsymbol{x}, t)$ at $\boldsymbol{x} = 0$, $\frac{1}{2}W_0$, W_0 and $2W_0$ are given in Figure 7b.

Considering next the radiation properties of this source one finds that if the parameters are chosen such that $c\bar{T}_0/b \ll 1$ then (29) generates a collimated pulsed beam (PB) field that propagates along the z-axis, having collimation length b and beamwidth $W(z) = W_0\sqrt{1 + z^2/b^2}$ so that for $z \gg b$ it expands along a constant diffraction angle $\Theta_0 = 0.64\sqrt{c\bar{T}_0/b} \ll 1$. (see e.g., [10], for a thorough review of PB fields see [8]).

In the examples below we choose $n = 2$ and $c\bar{T}_0/b = 0.001$. We design the point source array to realized the radiation pattern of the continuous distribution (29) subject to the error constraints $\epsilon = 0.01$ and $\bar{\epsilon} = 0.5$ (see (19)–(22)) within the cone whose angle Θ equals to the PB diffraction angle Θ_0. We shall compare the resulting array with an array designed to meet the error criteria within a wider cone $\theta \leq 3\Theta_0$.

The arrays have been designed using (25), (28) and the design considerations of Section 4.3. The cells have been rotated so that (η_1, η_2) coincide with the radial and azimuthal coordinates, respectively. Comparing (14) with (29), the parameters in (25) and (28) are $T_{n_1} = i\rho_n/bc$, $T_{n_2} = 0$ and $T_{n_{11}} = i/bc = T_{n_{22}}$ with $\rho_n = |\boldsymbol{x}_n|$.

Figure 2a depicts the inter element spacing $d_{n_{1,2}}$ (solid and dashed lines for the radial and azimuthal dimensions, respectively) as a function of the radial coordinate for the realization with $\Theta = \Theta_0$. All dimensions are normalized to W_0. The values $d_{n_{1,2}}$ that were actually chosen to minimize the number of elements are denoted by $\diamondsuit$ and $\bigcirc$. For $|\boldsymbol{x}| < 1.3W_0$, $d_{n_{1,2}}$ are relatively small and are determined by (28). For $|\boldsymbol{x}| > 1.3W_0$, the values obtained from (28) are larger than those obtained via (25) hence $d_{n_{1,2}}$ were calculated there via (25). Figure 2b depicts the array layout: the array is denser at the center and consists of a total of 44 elements within a circle of radius $4.7W_0$.

Figure 3 depicts the results for an array designed to meet the same error criteria within a wider cone $\Theta = 3\Theta_0$. The array dimensions were determined via (28) and (25) for $|\boldsymbol{x}| \lessgtr 0.87W_0$, respectively, giving a total number of 82 elements within a supporting radius $3.7W_0$.

Figure 4 depicts the far-zone pulse at several observation angles: The solid, the dotted and the dash-dotted lines correspond, respectively, to the continuous distribution and to the array realizations of Figures 2 and 3. One observes an excellent agreement for $\theta = 0$ and $\theta = \Theta_0$ (Figures 4a and 4b). For $\theta \geq 2\Theta_0$, i.e., beyond the design range of the array of Figure 2, the waveforms corresponding to that array break into the individual element contributionss (Figures 4c–4d; note the different scales in the figures). The conditions for

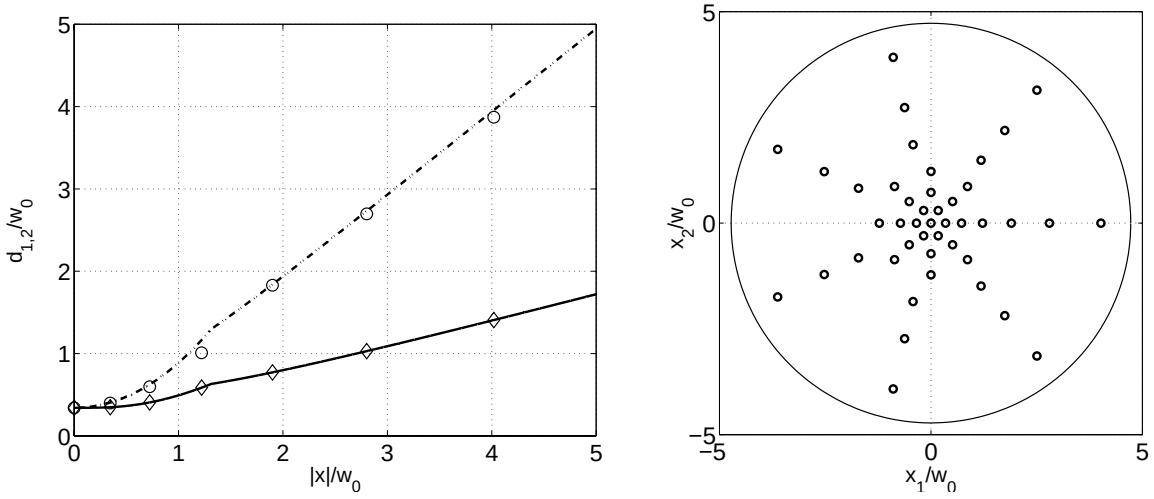

(a) (b)

Figure 2. Array realization for $\theta \leq \Theta_0$, $\epsilon = 0.01$ and $\bar{\epsilon} = 0.5$. (a). The inter-element spacing, d_1/W_0 (solid line) and d_2/W_0 (dash-dotted line) as a function of the radial coordinate: $\diamondsuit$ and $\bigcirc$ mark the values $d_{1,2}$ that were actually chosen. (b.) Array layout.

breaking of the pulse into the individual element contributions have been studied in [7] in connection with equi-spaced arrays. Similarly, the waveforms obtained from the array of Figure 3 break into the individual element contributions for $\theta \geq 4\Theta_0$ (Figures 4e–4f). Finally in Figure 5 we show the far zone pulse for large observation angles (further away from the main beam) where the pulse is broken to the individual element contributions. The relative realization error in this region is large yet it is negligible when compared to the main beam field.

Figure 6 depicts the energy radiation pattern, defined by $\|\widetilde{q}(\boldsymbol{\xi}, t)\|^2/\|\widetilde{q}(\mathbf{0}, t)\|^2$ with $\mathbb{L}_2$ norm. Consistently with the discussion above, the array patterns agree with the continuous source distribution in the design region $\theta < \Theta_0$ and $\theta < 3\Theta_0$ for the arrays in Figures 2 and 3, respectively. Beyond this range the patterns become flat since in this angular range the radiated fields break into non-overlapping individual pulse contributions (see Figure 5).

Finally, we compare our design with a design of an ultra wide band non-uniform array based on *frequency domain* considerations. In order to avoid grating lobes in the visible range, the local element spacing $d(\boldsymbol{x})$ at point $\boldsymbol{x}$ in the aperture plane is determined in this approach via

$$d(\boldsymbol{x}) \leq \lambda_c(\boldsymbol{x}) = 2\pi c/\omega_c(\boldsymbol{x}) \tag{33}$$

where $\omega_c(\boldsymbol{x})$ is the characteristic frequency of signal at $\boldsymbol{x}$. Recalling (30), the frequency spectrum of the source distribution in (29) with the pulse in (31) and $n = 2$ is given by

$$\widehat{q}(\boldsymbol{x}, \omega) = (-i\omega)^2 \exp(-\tfrac{1}{2}\omega T(\boldsymbol{x})), \qquad T(x) = \bar{T}_0 + |\boldsymbol{x}|^2/cb \tag{34}$$

One observes that the characteristic frequency of the excitation signal decreases as $|\boldsymbol{x}|$ increases (cf. Figure 7a that depicts the frequency spectrum at $\boldsymbol{x} = 0$ and at $|\boldsymbol{x}| = W_0$).

Figure 8 depicts the ratio $d_{1,2}(\boldsymbol{x})/d_c(\boldsymbol{x})$ between the element spacing obtained via the time-domain analysis in Figure 2 and between that obtained via the frequency-domain analysis. The time-domain design

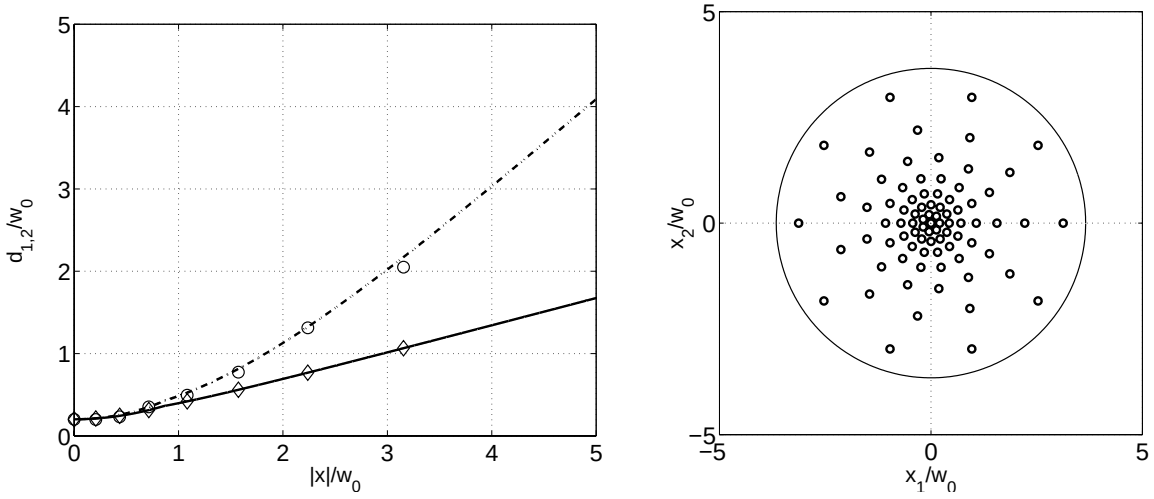

(a) (b)

Figure 3. As in Figure 2 for an array realization with $\theta \leq 3\Theta_0$.

is much sparser than the frequency domain design: The total number of elements in the former is 44 while in the latter there are $\sim$ 4500 elements. The difference stems from the fact that the time-domain design accounts for the actual signal and thus emphasizes the regions where this signal is meaningful. The frequency-domain design, on the other hand, is not based on the total field, but rather on kinematic concepts of phase interference at each frequency.

6. Concluding Remarks

We have considered a scheme for the design of sparse non-uniform point-source arrays that realize continuous source distributions within a given error criterion. The scheme is quite general and it leads to the sparsest array-realization for any given source distribution. The scheme can, in principle, be applied to scanning arrays but it has been demonstrated here only for realization of collimated short-pulse beam fields whose main bean direction is fixed along the z-axis. The error criterion has been imposed within a cone around this axis whereas outside this region the relative realization error is large yet it is negligible since the field there is small compared to the main beam field.

When the procedure above is applied to the construction of scanning arrays, the array sparsity is determined by the most restrictive constraints corresponding to all the possible scan directions within a given range. The analysis for each scan direction proceeds as in the example considered in above. One finds that the results are practically unchange; for an array that can stir the PB of Section 5 within a cone of angle $\theta_{\max}$ about the z axis, the size of the array should be increased by a factor $1/\cos\theta_{\max}$, so as to obtain the same effective aperture at the largest scan angle, but the interelement spacing should remain essentially the same so as to accommodate all the scan directions within the cone (see further discussion in Section 4.3). The examples in Section 5 deal, however, only with broadside radiating arrays while further analysis of scan arrays will be considered elsewhere.

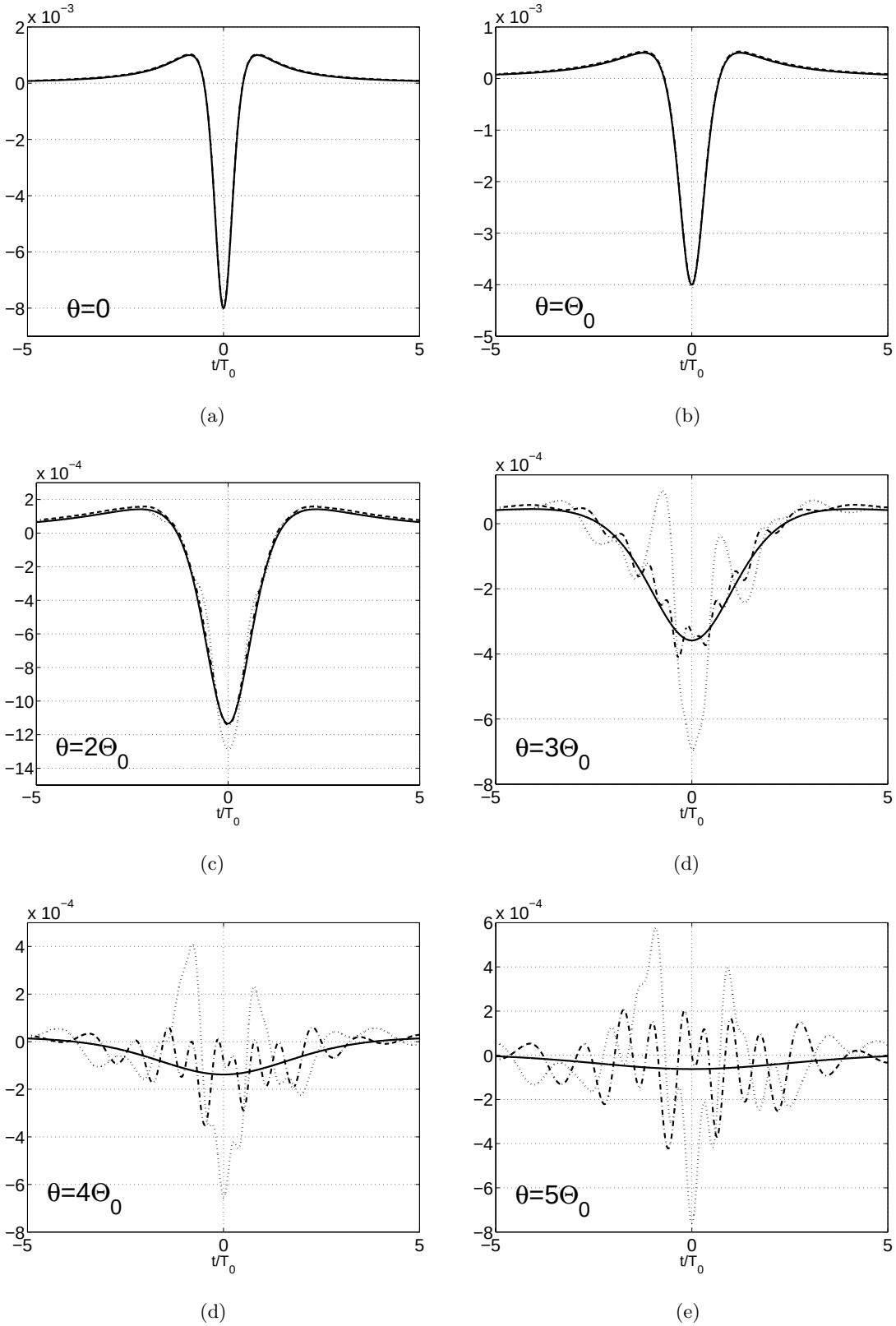

Figure 4. Far zone waveforms. Solid, dotted and dash-dotted lines: waveforms corresponding to the continuous source and to the array realizations in Figures 2 and 3, respectively. (a)–(f): Observation direction $\theta = 0$, Θ_0, $2\Theta_0$, $3\Theta_0$, $4\Theta_0$ and $5\Theta_0$.

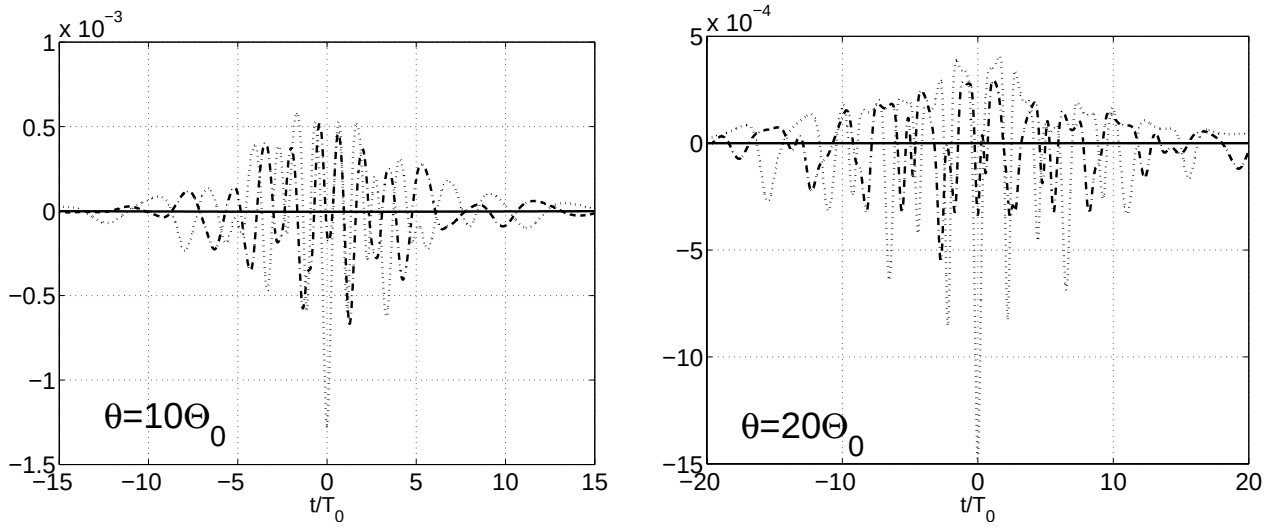

(a) (b)

Figure 5. Far zone waveforms, as in Figure 4 but for observation angles (a) $\theta = 10\Theta_0$ and (b) $\theta = 20\Theta_0$.

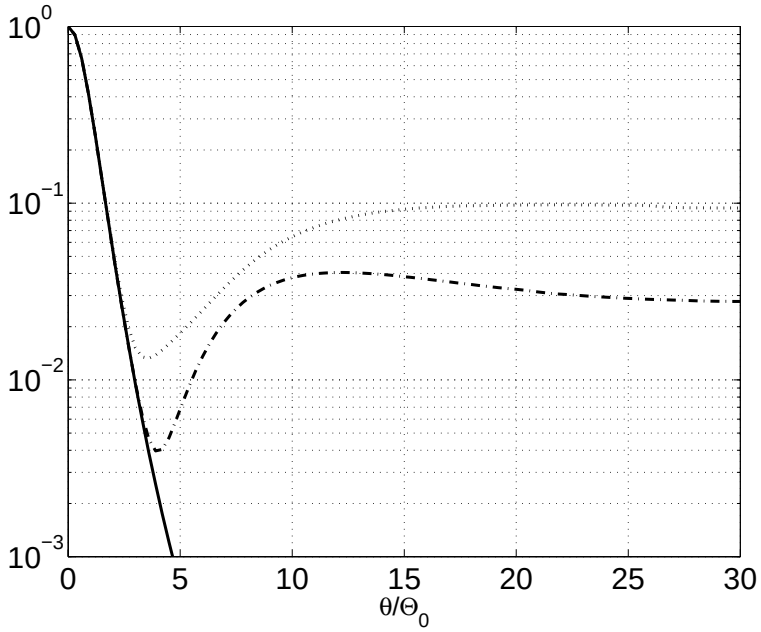

Figure 6. The energy radiation pattern as a function of θ corresponding to the waveforms in Figure 4.

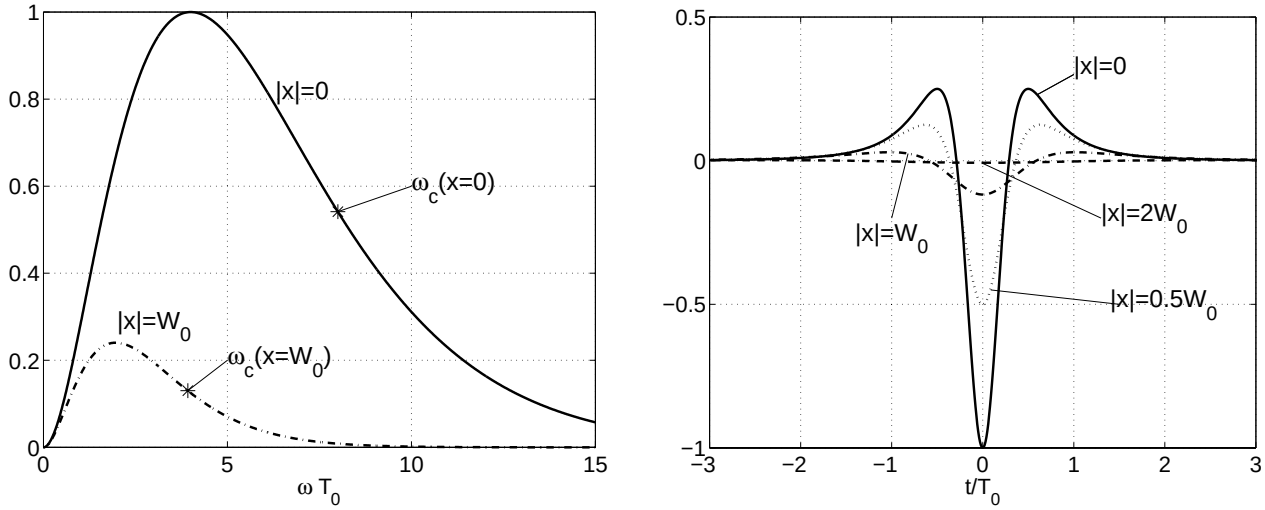

(a) (b)

Figure 7. Source distribution $q(\boldsymbol{x},t)$ of (29) with $n=2$ at $|\boldsymbol{x}|=0$ and at $|\boldsymbol{x}|=W_0$ (solid and dashed lines, respectively). (a) Frequency spectrum $\widehat{q}(\boldsymbol{x},\omega)$. (b) $q(\boldsymbol{x},t)$.

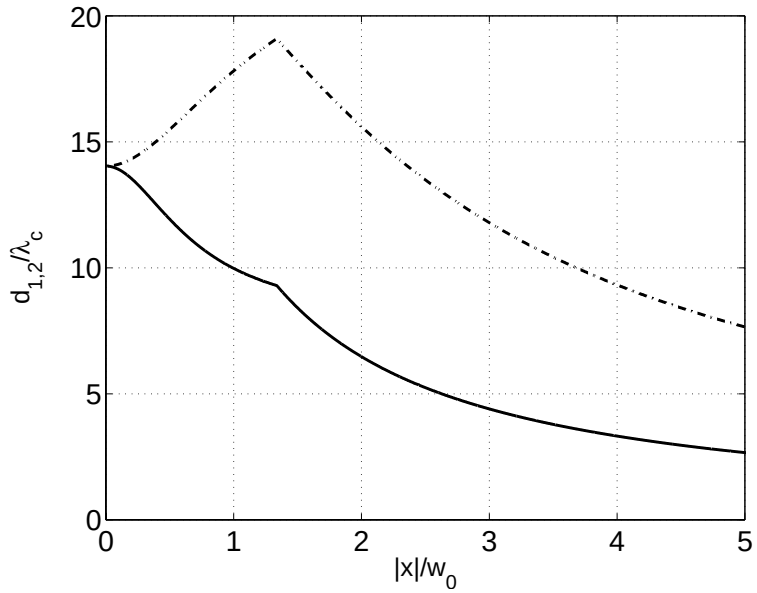

Figure 8. The ratio between the inter-element spacing $d_{1,2}(\boldsymbol{x})$ calculated via the time domain analysis and $d_c(\boldsymbol{x})$ calculated via the frequency domain criterion. d_1/d_c - solid line. d_2/d_c - dash-dotted line.

Acknowledgement

This work has been supported in part by the Israel Science Foundation under Grant No. 404/98, and in part by AFOSR Grant No. F49620-01-C-0018.

References

[1] F. Anderson, W. Christensen, F. Fullerton and B. Kortegaard, "Ultra-wideband beamforming in sparse arrays," *IEE Proceedings–H*, Vol. 138, pp. 342–346, August 1991.

[2] C. E. Baum, "Transient arrays," in *Proceedings of the Ultra-Wideband, Short-pulse Electromagnetics 3,* C. E. Baum et. al (eds), 129–138, 1997, Plenum Press, NY.

[3] P. Crombie P, P. A. J. Bascom and R. S. C Cobbold,"Calculating the pulsed response of linear arrays: Accuracy versus computational efficiency," *IEEE Trans. Ultrasonic ferroelectric and frequency control*, **UFFC-44**, 997–1009, 1997.

[4] J.L. Schwartz and B. D. Steinberg, "Ultrasparse, ultrawideband arrays," *IEEE Trans. Ultrasonic ferroelectric and frequency control*, **UFFC-45**, 376–393, 1998.

[5] D.T. McGrath and C.E. Baum, "Scanning and impedance properties of TEM horn arrays for transient radiation," *IEEE Trans. Antennas Propagat.*, **AP-47**, 469–473, 1999.

[6] B. Piwakowski and K. Sbai,"A new approach to calculate the field radiated from arbitrarily structured transducer arrays ," *IEEE Trans. Ultrasonic ferroelectric and frequency control*, **UFFC-46**, 422–440, 1999.

[7] A. Shlivinski and E. Heyman, "A unified kinematic theory of transient arrays," in *Proceedings of the Ultra-Wideband, Short-pulse Electromagnetics 5,* P.D Smith ed., June 2000, to be published by Plenum Press, NY.

[8] E. Heyman and L.B. Felsen, "Gaussian beam and pulsed beam dynamics: Complex source and spectrum formulations within and beyond paraxial asymptotics," *J. Opt. Soc. Am. A*, Vol. 18, pp. 1588–1611, July 2001.

[9] B.Z. Steinberg, E. Heyman and L.B. Felsen,"Phase space beam summation for time dependent radiation from large apertures: Continuous parametrization," *J. Opt. Soc. Am. A*, **8**, 943–958, 1991.

[10] E. Heyman and T. Melamed, "Certain consideration in aperture synthesis for ultra-wideband/short-pulsed fields," *IEEE Trans. Antennas Propagat.*, **AP-42**, 518–525, 1994.

[11] T. B. Hansen and A. D. Yaghjian, *Plane-Wave Theory of Time-Domain Fields: Near-Field Scanning Applications*, IEEE Press Series on Electromagnetic Wave Theory, New York (1999).

[12] E. Heyman, "Time-dependent plane-wave spectrum representation for radiation from volume source distributions," *J. Math. Phys.*, **37**, 658–681, 1996.